

# Multi-Electrostatic FPGA Placement Considering SLICEL-SLICEM Heterogeneity, Clock Feasibility, and Timing Optimization

Jing Mai, Jiarui Wang, Zhixiong Di *Member, IEEE*, Yibo Lin *Member, IEEE*

**Abstract**—When modern FPGA architecture becomes increasingly complicated, modern FPGA placement is a mixed optimization problem with multiple objectives, including wirelength, routability, timing closure, and clock feasibility. Typical FPGA devices nowadays consist of heterogeneous SLICEs like SLICEL and SLICEM. The resources of a SLICE can be configured to {LUT, FF, distributed RAM, SHIFT, CARRY}. Besides such heterogeneity, advanced FPGA architectures also bring complicated constraints like timing, clock routing, carry chain alignment, etc. The above heterogeneity and constraints impose increasing challenges to FPGA placement algorithms.

In this work, we propose a multi-electrostatic FPGA placer considering the aforementioned SLICEL-SLICEM heterogeneity under timing, clock routing and carry chain alignment constraints. We first propose an effective SLICEL-SLICEM heterogeneity model with a novel electrostatic-based density formulation. We also design a dynamically adjusted preconditioning and carry chain alignment technique to stabilize the optimization convergence. We then propose a timing-driven net weighting scheme to incorporate timing optimization. Finally, we put forward a nested Lagrangian relaxation-based placement framework to incorporate the optimization objectives of wirelength, routability, timing, and clock feasibility. Experimental results on both academic and industrial benchmarks demonstrate that our placer outperforms the state-of-the-art placers in quality and efficiency.

## I. INTRODUCTION

Placement is a critical step in the FPGA design flow, with a great impact on routability and timing closure. In the literature, three types of FPGA placement have been investigated: 1) partitioning-based, 2) simulated annealing (SA), and 3) analytical approaches [1], [2]. Partitioning-based approaches such as [3] usually have good scalability, but often fail to achieve high-quality results. SA-based approaches like the widely-adopted academic tool VPR [3] can achieve good results on small designs, but suffer from poor scalability on large designs. Recent studies have shown that analytical approaches [4]–[15] can achieve the best trade-off between quality and runtime. Thus modern FPGA placers mainly adopt analytical approaches in academia and industry.

The preliminary version has been presented at the Design Automation Conference (DAC) in 2022. This work was supported in part by the National Science Foundation of China (Grant No. 62034007 and No. 62141404) and the 111 Project (B18001).

J. Mai and J. Wang are with School of Computer Science, Peking University, Beijing, China.

Y. Lin is with School of Integrated Circuits, Peking University, Beijing, China. Corresponding author: Yibo Lin (yibolin@pku.edu.cn).

Z. Di is with School of Information Science and Technology, Southwest Jiaotong University, Chengdu, China.

Modern FPGA placement has two major challenges: 1) the heterogeneity of FPGA architecture, 2) the various constraints (e.g., timing, clock routing, chain alignment, etc.) imposed by advanced circuit designs [2], [16]–[18]. The heterogeneity of the FPGA architecture comes from the variety of instance types, the imbalance of resource distribution, and the asymmetric slice compatibility from the SLICEL-SLICEM heterogeneity [19]. The diversity of instance sizes and the inconsecutive site compatibility challenge the modern FPGA placement algorithms, which are mainly based on continuous optimization [2], [13].

Furthermore, solving the highly heterogeneous FPGA placement problem while satisfying advanced constraints has become more challenging [2]. i) Wire-induced delays are becoming the primary source of overall circuit delay [20]–[22]. Timing-driven placement is required to meet the aggressive timing constraints. However, the nonlinear and non-monotonic wire delays impose unique challenges to timing optimization in FPGA placement. ii) Modern FPGA adopts complicated clock architectures to achieve low clocking skew and high performance [16], [17]. Such a clock architecture introduces complicated clock routing constraints, increasing the challenges in FPGA placement. Therefore, clock-aware FPGA placement is required to accommodate the needs of modern FPGA design flows. iii) Modern FPGA needs to align the cascaded instances like CARRY into an aligned chain at the placement stage to boost performance. Such a chain alignment requirement induces large placement blocks and tends to degrade the quality of the solution.

In this work, we propose a state-of-the-art placement framework considering SLICEL-SLICEM heterogeneity and the co-optimization with wirelength, routability, clock feasibility, and timing optimization. We handle a comprehensive set of instance types, i.e., { LUT, FF, BRAM, distributed RAM, SHIFT, CARRY }, and cope with SLICEL-SLICEM heterogeneity based on a multi-electrostatic system. We propose a uniform non-linear optimization paradigm taking wirelength, routability, clock feasibility, and timing optimization into consideration from the perspective of *nested Lagrangian method*. The main contributions of this work are summarized as follows.

- We adopt an effective SLICEL-SLICEM heterogeneity model based on the division and assembly of electrostatic-based density formulation.
- We develop a dynamically adjusted preconditioning and carry chain alignment technique to stabilize the opti-

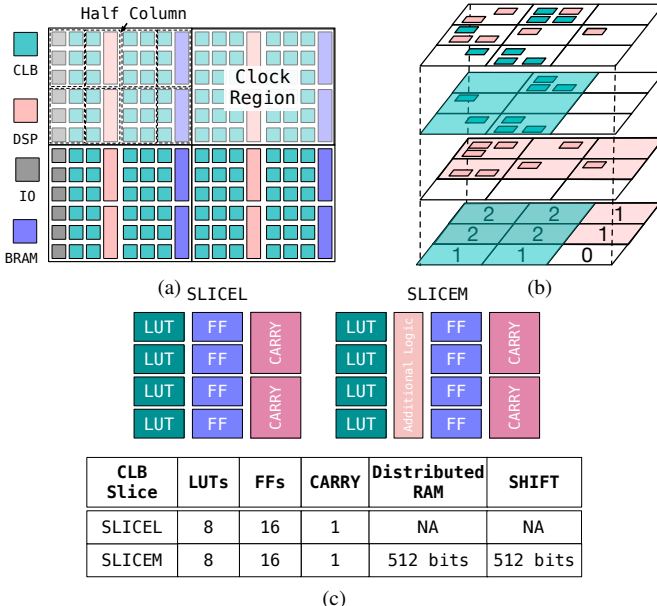


Fig. 1: (a) An example of a simplified vertical FPGA architecture depiction showing a  $2 \times 2$  clock region and half columns (dash lines) for *Xilinx UltraScale*. (b) An example of how the clock demand can be calculated. The different colors represent different clocks, and the numbers represent the clock demand of each CR. (c) An illustration of CLB slices classified into SLICEL and SLICEM with asymmetric compatibility. In a SLICEL, LUT blocks can be configured to be LUTs. A SLICEM can only be configured in *one* of the following modes: LUT, distributed RAM, or SHIFT. There is no mixing of LUTs, distributed RAMs, and SHIFTs in a CLB.

mization convergence and enable better final placement results.

- We cope with the time violation by an effective timing-criticality-based net weighting scheme, and incorporate the timing optimization into a continuous optimization algorithm.
- To achieve effective clock routing violation elimination, we adopt a instance-to-clock-region mapping considering the resource capacity of the clock regions and perturbation to the placement, and propose a quadratic clock penalty function in a continuous global placement engine with minor quality degradation.
- Putting the aforementioned techniques together, we put forward a nested Lagrangian relaxation framework incorporating the optimization objectives of wirelength, routability, timing, and clock feasibility.

Experiments on *ISPD 2017 contest benchmarks* demonstrate 14.2%, 11.7%, 9.6%, and 7.9% improvement in routed wirelength, compared to the recent cutting-edge FPGA placers [9]–[11], [15], respectively. Our placer also supports GPU acceleration and gains 1.45–6.58× speedup over the baselines. Further experiments on *industrial* benchmarks demonstrate that the proposed algorithms can achieve 23.6% better WNS, 22.5% better TNS with about 2% routed wirelength degradation compared with the conference version.

The rest of the paper is organized as follows. Section II introduces the preliminary knowledge of the FPGA architecture and modern FPGA placement. Section III details the core placement algorithms. Section IV shows the experimental results, followed by the conclusion in Section V.

## II. PRELIMINARIES

In this section, we primarily focus on the architecture of FPGAs and the methodology of multi-electrostatics-based FPGA placement.

### A. Device Architecture

In this work, we use the *Xilinx UltraScale* family [19], [25], e.g., the *UltraScale VU095* as a model FPGA design (illustrated in Fig. 1a). The *ISPD 2016* and *2017* FPGA placement challenges employed a condensed version of this architecture with a limited number of instance types, including LUT, FF, BRAM, and DSP [16], [17].

1) *SLICEL-SLICEM heterogeneity*: Shift registers (SHIFT) and distributed RAMs are two additional LUT-like instances of the architecture in addition to regular LUTs. Slices in CLBs fall into two categories: SLICEL and SLICEM, whose architectures are depicted in Fig. 1c. Due to the modest differences in logic resources, SLICEL and SLICEM support various configurations. LUTs, FFs, and CARRYs can be placed in both SLICEL and SLICEM. On the other hand, SHIFT and distributed RAMs can only be placed in SLICEM, which sets them apart from other common instances such as DSPs and BRAMs. Additionally, a SLICEM cannot be used as SHIFTs or distributed RAMs if it is configured as LUTs; vice versa.

2) *Carry Chain Alignment Constraints*: As a placement constraint for CARRY instances, we also need to take carry chain alignment into account. A carry chain is made up of several consecutive CARRY instances connected by cascaded wires from the lower bits to the upper bits, and the CARRY instances are arranged in CLB slices. According to the alignment constraint, each CARRY instance in a chain must be positioned in a single column and in subsequent slices in the correct sequence for the cascading wires.

3) *Clock Constraints*: The target FPGA device owns  $5 \times 8$  rectangular-shaped clock regions (CRs) in a grid manner, as shown in Fig. 1a.<sup>1</sup> Each CR is made up of columns of site resources and can be further horizontally subdivided into pairs of lower and upper half columns (HCs) of half-clock-region height. Except for a few corner cases, the width of each HC is the same as that of two site columns, as shown in Fig. 1a. All the clock sinks within a half column are driven by the same leaf clock tracks.

The clock routing architecture imposes two clock constraints on placement, i.e., the *clock region constraint* and the *half column constraint*, as shown in Fig. 1b. The clock region constraint limits each clock region's clock demand to a maximum of 24 clock nets, where the clock demand is the

<sup>1</sup>Fig. 1a only contains part of the whole  $5 \times 8$  CRs, but is sufficient for illustration.

TABLE I: Features of the published state-of-the-art FPGA placers.

Placer	RippleFPGA [23]	GPlace [7]	UTPlaceF [5]	elfPlace [13]	FTPPlace [20]	GPlace 3.0 [24]	RippleFPGA Clock-Aware [11]	UTPlaceF 2.0&2.X [9], [10]	NTUFPlace [15]	Lin <i>et al.</i> [21]	Ours
Clock Constraints	×	×	×	×	×	×	✓	✓	✓	✓	✓
Resources Supported	LUT, FF, BRAM, DSP	✓	✓	✓	✓	✓	✓	✓	✓	✓	✓
	CARRY, SHIFT, Distributed RAM	×	×	×	×	×	×	×	×	×	✓
Timing Optimization	×	×	×	×	✓	×	×	×	×	✓	✓
GPU-Acceleration	×	×	×	✓	×	×	×	×	×	×	✓
Algorithm Category	Quadratic	Quadratic	Quadratic	Nolinear	Quadratic	Quadratic	Quadratic	Quadratic	Nonlinear	Nonlinear	Nonlinear

total number of clock nets whose bounding boxes intersect with the clock region. The half-column constraint limits the number of clock nets within the half-column to a maximum of 12.

### B. Multi-Electrostatics based FPGA Placement

As shown in Fig. 2, electrostatics-based placement models each instance as an electric particle in an electrostatic system. As firstly stated in the ASIC placement [26], *minimizing potential energy* can resolve density overflow in the layout. The principle is based on the fundamental physical insight that a balanced charge distribution in an electrostatic system contributes to low potential energy, so *minimizing potential energy can resolve density overflow and help spread instances in the layout*. We are also extending this approach to the use of multiple electrostatic fields, which will enable multiple types of resource to be handled in FPGA placement, such as LUTs, FFs, DSPs, and BRAMs. Fig. 3 illustrates a multi-electrostatic formulation of LUTs and DSPs. In order to reduce density overflow, we must minimize the total potential energy of multiple fields because low energy means a balanced distribution of instances. The issue can be summarized as follows.

$$\min_{\mathbf{x}, \mathbf{y}} \widetilde{W}(\mathbf{x}, \mathbf{y}) \quad \text{s.t. } \Phi_s(\mathbf{x}, \mathbf{y}) = 0, \quad (1)$$

where  $\widetilde{W}(\cdot)$  is the wirelength objective,  $\mathbf{x}, \mathbf{y}$  are instance locations,  $S$  denotes the field type set, and  $\Phi_s(\cdot)$  is the electric potential energy for field type  $s \in S$ . Formally, we constrain the target potential energy of each field type to be zero, though the energy is usually non-negative. The constraints can be further relaxed to the objective and guide the instances to spread out. Practically, we stop the optimization when the energy is small enough; or equivalently, the density overflow is low enough. Notice that the formulation in Fig. 3 assumes that one instance occupies the resources of only one field, which cannot handle the complicated SLICEL-SLICEM heterogeneity shown in Section II-A1.

### C. Timing Optimization

Timing-driven placement imposes more concern about timing closure than the total wirelength objective in wirelength-driven placement. Worst negative slack (WNS) and total negative slack (TNS) are two widely adopted timing metrics. WNS is the maximum negative slack among all timing paths in the design, and TNS is the sum of all negative slacks of timing endpoints. Thus, WNS and TNS are used to evaluate the timing performance of a design from the worst and the global view respectively, and the smaller the WNS and TNS

are, the worse the timing performance is. The timing-driven placement problem can be formulated as follows.

$$\min_{\mathbf{x}, \mathbf{y}} \mathcal{T}(\mathbf{x}, \mathbf{y}), \quad (2a)$$

$$\text{s.t. } \rho_s(\mathbf{x}, \mathbf{y}) \leq \hat{\rho}_s, \quad \forall s \in S, \quad (2b)$$

where  $S$  is the instance type set,  $\rho_s(\cdot)$  denotes the density for instance type  $s \in S$ , and  $\hat{\rho}_s$  represents the target density for instance type  $s \in S$ . The objective function  $\mathcal{T}(\cdot)$  can be WNS, TNS, or the weighted sum of both. Improving TNS requires collaborative optimization of all timing paths, and is therefore suitable for the global placement stage. On the other hand, WNS is more suitable for the detailed placement stage, as it only considers the worst timing path. It is worth noting that directly solving Eq. (2) is very difficult, because the delay model generally has strong discrete and non-convex properties [27]. Therefore, we draw on the two intuitive elements of wirelength-driven placement and static timing analysis, i.e., net weights and slacks, to tackle this problem.

### D. Problem Formulation

TABLE I summarizes the characteristics of the published state-of-the-art FPGA placers. In recent years, modern FPGA placers mainly resort to quadratic programming-based approaches [4]–[12] and nonlinear optimization-based approaches [13]–[15] for the best trade-off between quality and efficiency. Among them, the current state-of-the-art quality is achieved by nonlinear approaches *elfPlace* [13] and *NTUFPlace* [15], whose instance density models are derived from a multi-electrostatics system and a hand-crafted bell-shaped field system. However, most existing FPGA placers only consider a simplified FPGA architecture, i.e., LUT, FF, DSP, and BRAM, ignoring the commonplace SLICEL-SLICEM heterogeneity in real FPGA architectures [5]–[11], [13]–[15]. Among these placers, only a few placers utilize the parallelism that the GPU provides [13], and few consider timing and clock feasibility in practice [8], [9], [11], [14], [15].

In this work, we aim at optimizing wirelength, timing, and routability while cooperating with SLICEL-SLICEM heterogeneity, alignment feasibility, and clock constraints. We define the FPGA placement problem as follows.

**Problem 1** (FPGA Placement). *Taking as input a netlist consisting of LUTs, FFs, DSPs, BRAMs, distributed RAMs, SHIFTs, and CARRYs, generate a plausible FPGA placement solution with optimized wirelength, timings, and routings, satisfying the requirements for alignment feasibility and meeting the clock constraints.*

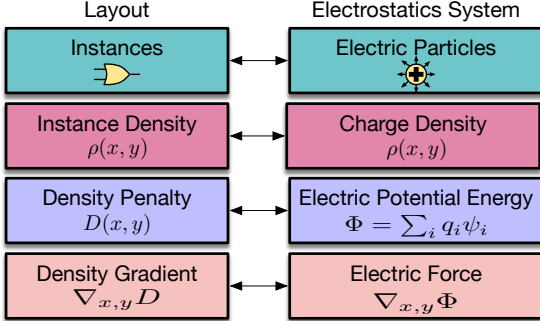


Fig. 2: Analogy between placement for a single resource type and an electrostatic system [28].

### III. ALGORITHMS

We will detail the placement algorithm in this section.

#### A. Overview of the Proposed Algorithm

As illustrated in Fig. 4, our method includes two fundamental stages: (1) nested global placement with timing awareness and clock feasibility, and (2) clock-aware legalization and detailed placement.

We cope with the SLICEL-SLICEM heterogeneity by defining the field type set as  $S = \{\text{LUTL, LUTM-AL, FF, CARRY, DSP, BRAM}\}$  with a special field setup (Section III-B). With clock constraints, carry chain alignment feasibility, and timing optimization, we formulate the problem as Formulation (3).

$$\min_{\mathbf{x}, \mathbf{y}} \tilde{\mathcal{T}}_{\omega}(\mathbf{x}, \mathbf{y}), \quad (3a)$$

$$\text{s.t. } \Phi_s(\mathbf{x}, \mathbf{y}; \mathcal{A}^s) = 0, \quad \forall s \in S, \quad (3b)$$

$$\Gamma(\mathbf{x}, \mathbf{y}) = 0, \quad (3c)$$

$$\text{Carry chain alignment constraint,} \quad (3d)$$

$\tilde{\mathcal{T}}_{\omega}(\cdot)$  is the timing performance objective, where  $\omega$  measures the net criticality in the current timing graph (Section III-F).  $\mathcal{A}^s$  denotes the instance areas in the field  $s$ , and  $\Gamma(\cdot)$  is the clock penalty term (Section III-E). For brevity, in later discussions, we condense  $\Phi_s(\mathbf{x}, \mathbf{y}; \mathcal{A}^s)$  to  $\Phi_s$  for all  $s \in S$ , and denote  $\Phi$  as the potential energy vector, whose components are the potential energy for each field, i.e.,  $\Phi_s (\forall s \in S)$ .

We relax the original problem (3) by leveraging the *augmented Lagrangian method (ALM)* [29] to formulate a better unconstrained subproblem,

$$\begin{aligned} \min_{\mathbf{x}, \mathbf{y}} \quad & \mathcal{L}(\mathbf{x}, \mathbf{y}; \boldsymbol{\lambda}, \mathcal{A}, \eta, \omega) = \tilde{\mathcal{T}}_{\omega}(\mathbf{x}, \mathbf{y}) + \sum_{s \in S} \lambda_s \mathcal{D}_s \\ & + \eta \Gamma(\mathbf{x}, \mathbf{y}), \end{aligned} \quad (4a)$$

$$\mathcal{D}_s = \Phi_s + \frac{1}{2} \mathcal{C}_s \Phi_s^2, \quad \forall s \in S, \quad (4b)$$

The density multiplier vector is  $\boldsymbol{\lambda} \in \mathbb{R}^{|S|}$ , and the clock penalty multiplier is  $\eta \in \mathbb{R}$ . The purpose of the weighting coefficient vector  $\mathcal{C} \in \mathbb{R}^{|S|}$  is to achieve a balance between the first-order and second-order terms for density penalty. We follow the setup for  $\boldsymbol{\lambda}$  and  $\mathcal{C}$  as [13]. To cope with

multiple constraints, we rewrite the problem in a nested manner through the Lagrangian relaxation method,

$$\text{Timing Opt.: } \mathcal{L}_1 = \max_{\omega} \mathcal{L}_2(\omega), \quad (5a)$$

$$\text{Clock Opt.: } \mathcal{L}_2(\omega) = \max_{\eta} \mathcal{L}_3(\eta, \omega), \quad (5b)$$

$$\text{Routability Opt.: } \mathcal{L}_3(\eta, \omega) = \max_{\mathcal{A}} \mathcal{L}_4(\mathcal{A}, \eta, \omega), \quad (5c)$$

$$\text{Wirelength Opt.: } \mathcal{L}_4(\mathcal{A}, \eta, \omega) = \max_{\boldsymbol{\lambda}} \mathcal{L}_5(\boldsymbol{\lambda}, \mathcal{A}, \eta, \omega), \quad (5d)$$

$$\text{Subproblem: } \mathcal{L}_5(\boldsymbol{\lambda}, \mathcal{A}, \eta, \omega) = \min_{\mathbf{x}, \mathbf{y}} \mathcal{L}(\mathbf{x}, \mathbf{y}; \boldsymbol{\lambda}, \mathcal{A}, \eta, \omega), \quad (5e)$$

where  $\mathcal{L}_5$  denotes Eq. (4). To put it simply, a set of variables in the objective function is constrained to be the optimal solution of the extra optimization problem, and the variables of the exterior optimization problem are passed toward the sub-problem as fixed parameters. To illustrate, take the solving process of  $\mathcal{L}_5$  as an example. The subproblem  $\mathcal{L}_5$  aims at finding the optimal instance positions  $\mathbf{x}$  and  $\mathbf{y}$  given a set of fixed parameters  $\boldsymbol{\lambda}$ ,  $\mathcal{A}$ ,  $\eta$ , and  $\omega$  from  $\mathcal{L}_4$ . When  $\mathcal{L}_5$  comes to the convergence to its minimum solution, the  $\mathcal{L}_4$  optimizer will improve the parameter  $\boldsymbol{\lambda}$  so as to enlarge the magnitude of the density terms in the overall optimization objectives. Therefore, the  $\mathcal{L}_5$  optimizer will try to find a better solution by moving the instances to a less dense region in a new iteration, and thus the density constraints will be forced to be gradually adequate. We also adopt the same procedure to solve the other subproblems.

Fig. 4 depicts the nested loops to solve the problem.  $\mathcal{L}_1$  aims at improving the timing slacks via the timing-criticality-based weighting method. The stopping criterion of  $\mathcal{L}_1$  is whether timing slacks can be improved (Section III-F).  $\mathcal{L}_2$  (Section III-E) aims at excluding the cases where clock routing is illegal under an analytical formulation. We regard  $\mathcal{L}_2$  as converged when there is no clock violation (Section II-A3).  $\mathcal{L}_3$  develops the area inflation-based technique from [13] in order to optimize the routability, and the estimated routing congestion and pin density are the convergence criteria of  $\mathcal{L}_3$ .  $\mathcal{L}_4$  is the core wirelength-driven placement problem. We empirically find that the density *overflow* is a good indicator of the density constraints.<sup>2</sup> For  $\mathcal{L}_5$ , we always solve with a fixed number of iterations, e.g., one iteration in the experiments.

In each iteration, we resolve the carry chain alignment constraints through iterative support from *iterative carry chain alignment correction* (Section III-D). Following placement, we evolve clock-aware direct legalization and detailed placement algorithms that above clock feasibility constraints are met [8]. We do not include details on routability optimization, clock-aware legalization, or detailed placement for brevity.

#### B. Multi-Electrostatic Model for SLICEL-SLICEM Heterogeneity

SLICEMs can operate in one of three modes: LUT, distributed RAM, or SHIFT, as discussed in Section II-A1. In

<sup>2</sup>We set the overflow threshold for LUTs and FFs to 10% in our experiments.

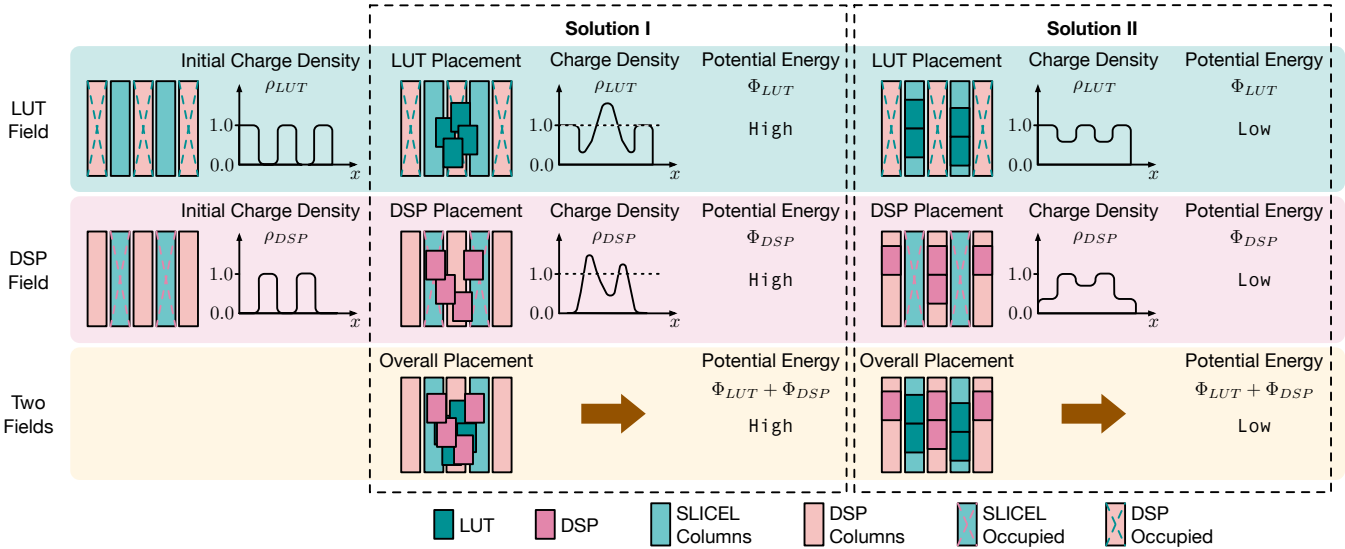


Fig. 3: An example of a multi-electrostatic formulation for LUT and DSP resources, which correspond to two electric fields. Unavailable columns are treated as occupied when calculating the initial charge density for each field. Take DSP as an example. Density overflow can occur if a DSP instance is not put in a DSP column or if there are overlaps between DSP instances, resulting in an uneven density distribution of the field and, finally, excessive electric potential energy. As a result, limiting energy in the layout can assist in the resolution of density overflow and spread cases. If we face density underflow ( $< 1.0$ ), we can insert fillers with positive charges for each field to fill the vacant spaces, [13], [26]. As a result, only density overflow will provide considerable potential energy. We may handle them in the same way by including FF and BRAM fields.

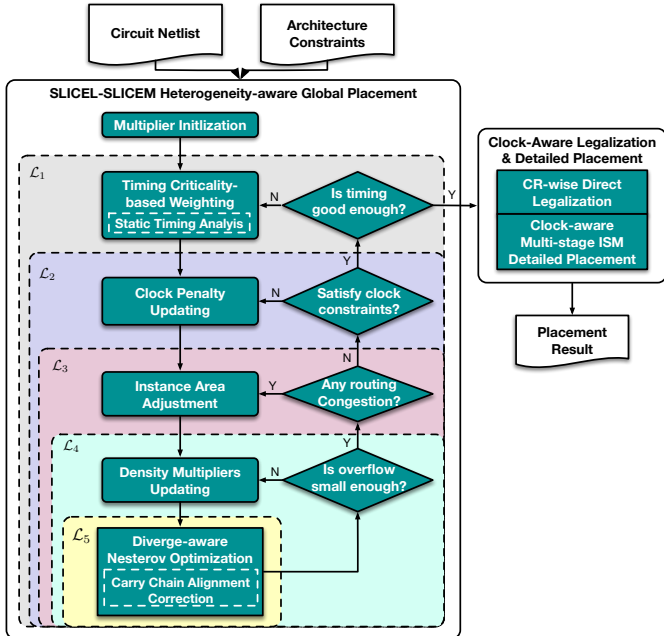


Fig. 4: The proposed Overall Flow.

the LUT slots of that SLICEM, only instances that match the mode can be placed. In order to address this constraint, we introduce two electrostatic fields,  $LUTL$  and  $LUTM-AL$ , into the multi-electrostatic placement model. In the field setup, it should be possible to prevent distributed RAM instances or SHIFT instances from being placed on SLICEL sites, however, it should be possible to place LUT instances both on SLICEL and SLICEM sites, as part of the field setup.

There is an example of how these two fields are set up in Fig. 5.  $LUTL$  models the LUT resources that are provided by

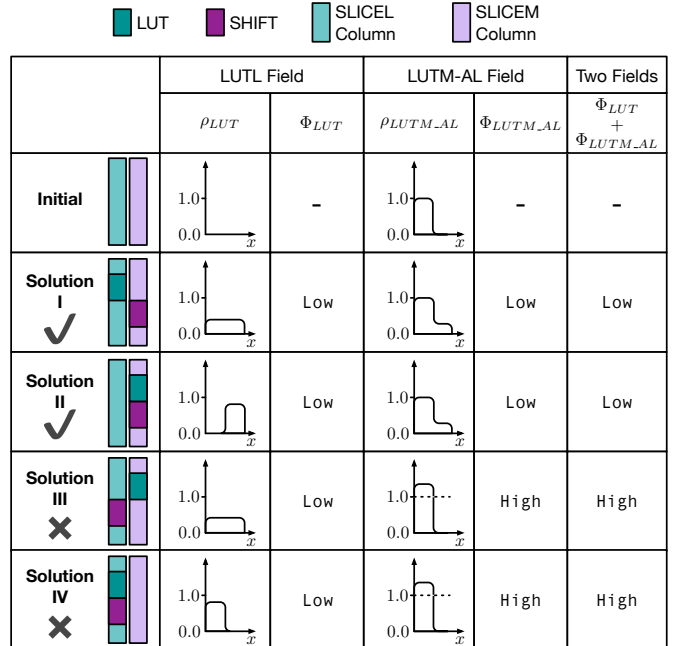


Fig. 5: As an example, here is a special electrostatic field setup that handles asymmetric slice compatibility as a result of SLICEL-SLICEM heterogeneity.  $LUTM-AL$  fields are prone to overflowing density due to the SHIFT instance placed on the SLICEL column in Solution III and IV. This results in high potential energy in the  $LUTM-AL$  field.

both SLICEM and SLICEL, whereas  $LUTM-AL$  models the additional logic resources that are supplied by SLICEM but not by SLICEL. In contrast to a distributed RAM or SHIFT

instance, a LUT instance only occupies resources within the LUTL field, while a distributed RAM or SHIFT instance occupies resources both in the LUTL and LUTM-AL fields.

Using an example of a LUT instance and a SHIFT instance as an example, this figure analyses four scenarios. As with SHIFT instances, distributed RAM instances work in exactly the same way. In order to indicate that a SLICEL does not contain any resources for LUTM-AL, we set the initial density for LUTM-AL in a SLICEL to 1, indicating the SLICEL is occupied; in contrast, the initial density for LUTL in a SLICEL is set to 0. We set the initial density of a SLICEM to zero for both LUTL and LUTM-AL due to the fact that it contains both LUTL and LUTM-AL resources. In Solution I, if the LUT instance is placed on a SLICEL and the SHIFT instance is placed on a SLICEM, there will be no overflow of density in either of the fields (a balanced density distribution can be achieved by inserting fillers [26]), which means that the potential energy will be minimized. In Solution II, the scenario is similar to the one in Solution I. Solution III and IV, on the other hand, where the SHIFT instance is placed on a SLICEL, produce a density overflow in the LUTM-AL field, which indicates that there is a high potential energy for this field. As long as the optimizer minimizes the potential energy, these solutions will be avoided. As a result, these two elaborate fields are able to accommodate LUT and distributed RAM/SIFT to their compatible sites in an easy manner.

### C. Divergence-aware Preconditioning

It is important to precondition the gradient  $\nabla \mathcal{L}^{(t)}$  for each iteration  $t$  before it is fed to the optimizer, where  $\mathcal{L}$  is the Lagrangian problem defined in Eq. (4). A gradient is discussed only in the direction of  $x$ , and a gradient in the direction of  $y$  is the same. To make the Jacobi preconditioner  $\mathcal{P}$  more efficient, we approximate the second-order derivatives of wirelength and density according to the following formula.

$$\mathcal{P}_i^W = \frac{\partial^2 \tilde{\mathcal{T}}_\omega(\mathbf{x}, \mathbf{y})}{\partial x_i^2} \sim \sum_{e \in E_i} \frac{w_e}{|e| - 1}, \quad \forall i \in \mathcal{V}, \quad (6a)$$

$$\mathcal{P}_i^{(t)} \sim \max \left( 1, \left[ \mathcal{P}_i^W + \sum_{s \in S} \alpha_s^{(t)} \lambda_s^{(t)} \mathcal{A}_i^s \right]^{-1} \right), \quad (6b)$$

In the above equation,  $\mathcal{V}$  denotes the set of instances,  $E_i$  denotes the nets incident to instance  $i \in \mathcal{V}$ ,  $w_e \in \omega$  denotes the weight of net  $e$ , and  $\mathcal{P}^W$  denotes the second-order derivative of the wirelength term. To optimize the model, we provide the optimizer with the preconditioned gradient  $\hat{\nabla} \mathcal{L}^{(t)} = \nabla \mathcal{L}^{(t)} \odot \mathcal{P}^{(t)}$ .

As shown in Fig. 6, after the loss surfaces have been preconditioned, they are now more isotropic and therefore can be optimized more rapidly. The intuition from the partial derivative itself is that we would expect that for  $\mathcal{P}_i^W$  instances with more pins or pins incident to larger net weights, they would move slower than instances with fewer pins, and for instances with larger  $\sum_{s \in S} \alpha_s^{(t)} \lambda_s^{(t)} \mathcal{A}_i^s$  would also move slower.

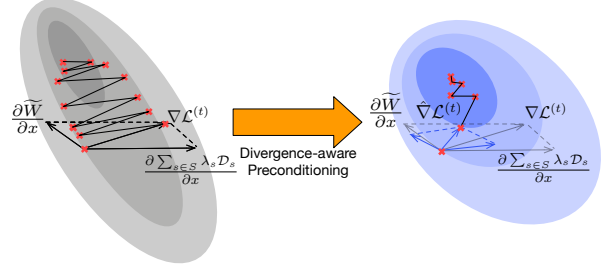


Fig. 6: It is shown in the figure how preconditioning takes place at iteration  $t$ . A preconditioning technique translates objection surfaces into a more isotropic form, and this leads to a reduction in iterations and a stabilization of the optimization process as a result.

It has been observed that if the ratio of the gradient norms from the density term and the wirelength term becomes too large, the optimization can diverge easily [13], [30]. Thus, we introduce an additional weighting vector  $\alpha \in \mathbb{R}^{|S|}$ , so that we can dynamically control the gradient norm ratio. It is illustrated in Fig. 6 that some instances are dominated by the density gradient, resulting in some instances moving too fast, and this causes the instances to diverge from each other. In most cases, this occurs during the second half of the placement iteration when the density term starts to compete with the wirelength term by increasing  $\lambda$  to maintain its position in front of it. In order to stabilize the optimization process, we need a new preconditioner. For convenience, we define two auxiliary variables  $\vartheta^{(t)}$  and  $\bar{\mathcal{P}}^W$ . Taking the gradient norms of the density and wirelength terms to be equal, we can derive  $\alpha$  as follows.

$$\vartheta_s^{(t)} = \max \left( 1, \frac{\nabla \mathcal{D}_s}{\sum_{i \in \mathcal{V}_s^r} |\partial \tilde{\mathcal{T}}_\omega / \partial x_i|} \right), \quad \forall s \in S, \quad (7a)$$

$$\bar{\mathcal{P}}_s^W = \frac{\sum_{i \in \mathcal{V}_s^r} \mathcal{P}_i^W}{|\mathcal{V}_s^r|}, \quad \forall s \in S, \quad (7b)$$

$$\alpha^{(t)} = \vartheta^{(t)} \odot \bar{\mathcal{P}}^W, \quad (7c)$$

$\mathcal{V}_s^r$  denotes the set of instances that have a demand in the field  $s$ .  $\sum_{i \in \mathcal{V}_s^r} |\partial \tilde{\mathcal{T}}_\omega / \partial x_i|$  is the wirelength gradient norm summation of  $\mathcal{V}_s^r$ . The weighting vector  $\vartheta^{(t)} \in \mathbb{R}^{|S|}$  measures the gradient norm ratio between the density term and the wirelength term, and  $\bar{\mathcal{P}}^W$  denotes the average wirelength preconditioner for each field type. The detailed derivations have been omitted for brevity. Experiments will be conducted to further validate its effectiveness.

### D. Iterative Carry Chain Alignment Correction

Using a carry chain alignment technique, we propose a method that can better align the carry chains without affecting the effectiveness of the analytical global placement algorithm. We move the sequential CARRYs together at the end of each global placement iteration, align them based on their horizontal coordinates, and then move them into a column shape at the end of an iteration. The CARRY instances in a chain will

move together during the global placement iterations, which eases the legalization step, since the chains will almost align once the global placement process is completed.

### E. Clock Network Planning Algorithm

There is a high degree of dissimilarity in the clock constraints in Section II-A3. The slightest movement within the clock region boundaries can result in an illegal clock configuration, which is detrimental to optimization. In order to simplify the clock planning process, we decompose it into two stages. Our first step is to find an *instance-to-clock-region mapping* in the first stage. This mapping ensures that all clock region constraints will be satisfied as long as all instances are located within the target clock region during the mapping. The second step involves moving all instances to their target clock regions by adding a penalty term to the placement objective, which is  $\Gamma(\cdot)$ . Following the global placement, the half-column constraints are then dealt with in the developed clock-aware direct legalization and detailed placement algorithm [8]. As we move forward, we will explain these two stages in more detail.

1) *Instance-to-Clock-Region Mapping Generation*: It is the goal of this step to generate mappings in a manner that ensures that clock constraints can be met with the minimum perturbation to the placement. As discussed in [10], we propose using *branch-and-bound method* to search through the solution space arising from different instance-to-clock-region mappings, and find a feasible solution with high quality within the solution space. As part of the second stage, we enlist the assignment that has the lowest cost and uses it as a base.

2) *The Clock Penalty for Placement*: In contrast to [9], [11], which forces instances to move directly to their clock regions, we introduce a bowl-like, smooth, and differentiable gravitational attraction term, which draws instances to the clock regions to which they have been mapped. Let  $lo_i^x$ ,  $hi_i^x$ ,  $lo_i^y$ , and  $hi_i^y$  be the left, right, bottom, and top boundary coordinates of the generated mapping result of instance  $i$ . We define the penalty term for instance  $i$  as  $\Gamma_i(\mathbf{x}_i, \mathbf{y}_i) = \Gamma_i(\mathbf{x}_i, \mathbf{y}_i)^x + \Gamma_i(\mathbf{x}_i, \mathbf{y}_i)^y$ , where  $\Gamma_i(\mathbf{x}_i, \mathbf{y}_i)^x$  is defined as,

$$\Gamma_i(\mathbf{x}_i, \mathbf{y}_i)^x = \begin{cases} (\mathbf{x}_i - lo_i^x)^2, & \mathbf{x}_i < lo_i^x, \\ 0, & lo_i^x \leq \mathbf{x}_i \leq hi_i^x, \\ (\mathbf{x}_i - hi_i^x)^2, & hi_i^x < \mathbf{x}_i. \end{cases} \quad (8)$$

A visual representation of the clock penalty term can be found in Fig. 7.  $\Gamma(\mathbf{x}, \mathbf{y})$  in Eq. (3) indicates that the sum of the clock penalty of all instances, i.e.,  $\Gamma(\mathbf{x}, \mathbf{y})$  is equal to  $\sum_{i \in \mathcal{V}} \Gamma_i(x_i, y_i)$ .

Initially, the clock penalty multiplier  $\eta$  is set to a value of 0. As soon as we reset the clock penalty function  $\Gamma(\cdot)$ , we update  $\eta$  with the relative ratio between the gradient norms of the wirelength and the clock penalty in order to maintain the stability of the clock penalty function.

$$\eta = \frac{\iota \|\nabla \widetilde{\Gamma}_\omega\|_1}{\|\nabla \Gamma\|_1 + \varepsilon}. \quad (9)$$

As we observe, only 1% of the instances are out of their available clock regions right after they have been assigned

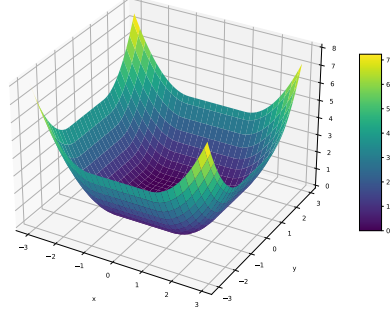


Fig. 7: The Visualization of clock penalty function  $\Gamma_i(\cdot)$  for a single instance.

the clock region, so most instances have no penalties as a result of this. It is empirically established that  $\iota$  is equal to  $10^{-4}$  and  $\varepsilon$  is equal to  $10^{-2}$  as a method of balancing the gradient norm ratio.

### F. Timing-Criticality-based Weighting Method

The timing performance objective  $\widetilde{\Gamma}_\omega(\cdot)$  (see Eq. (3)) consists of two components: i) the wirelength objective as a first-order approximation of WNS and TNS, and ii) the net criticality  $\omega$  that remedies the lack of timing information for first-order approximation.

$$\widetilde{\Gamma}_\omega(\mathbf{x}, \mathbf{y}) = \sum_{e \in E} \omega_e \cdot \widetilde{W}(e) \quad (10)$$

$\omega_e \in \omega$  measures the timing criticality of nets, i.e., whether any timing path through nets violates timing constraints, what is the degree of the violation, and how much the path delay can be reduced. In this section we detail how  $\widetilde{\Gamma}(\cdot)$  functions.

1) *Static Timing Analysis*: Timing-driven placement leverages the static timing analysis (STA) to evaluate the timing criticality of nets. STA relies on (i) model of signal delays for nets and instances, and (ii) a timing analysis engine based on net and instance delays.

Delay models in FPGA are highly coupled with the pre-fabricated routing architecture and the behavior of the FPGA router. In our experiment, we design the linear delay model, where the delay of the routing path between a source endpoint and a sink endpoint is calculated by the Manhattan distance between them. Given the delay of the timing edges, the timing analysis engine determines which timing paths violate their timing constraints. A timing path  $\pi$  is a directed acyclic path for particular source and sink pairs (primary I/Os and I/Os of store elements). The delay  $t_\pi$  along a path  $\pi$  is the sum of wire delays and cell delays, and every path comes with a timing constraint  $c_\pi$  defined via the *actual arrival time* (AAT) and *required arrival time* (RAT) for every driver pin and primary output.

The slack  $s_\pi$  of a path  $\pi$  is defined as  $s_\pi = c_\pi - t_\pi$ . We mainly focus on the *setup time* constraint, which is defined as the difference between the AAT and RAT. A timing path  $\pi$  violates the setup time constraints if the slack is negative. The slack of a timing edge is the smallest path slack among the paths containing this edge. To avoid enumerating all paths, we

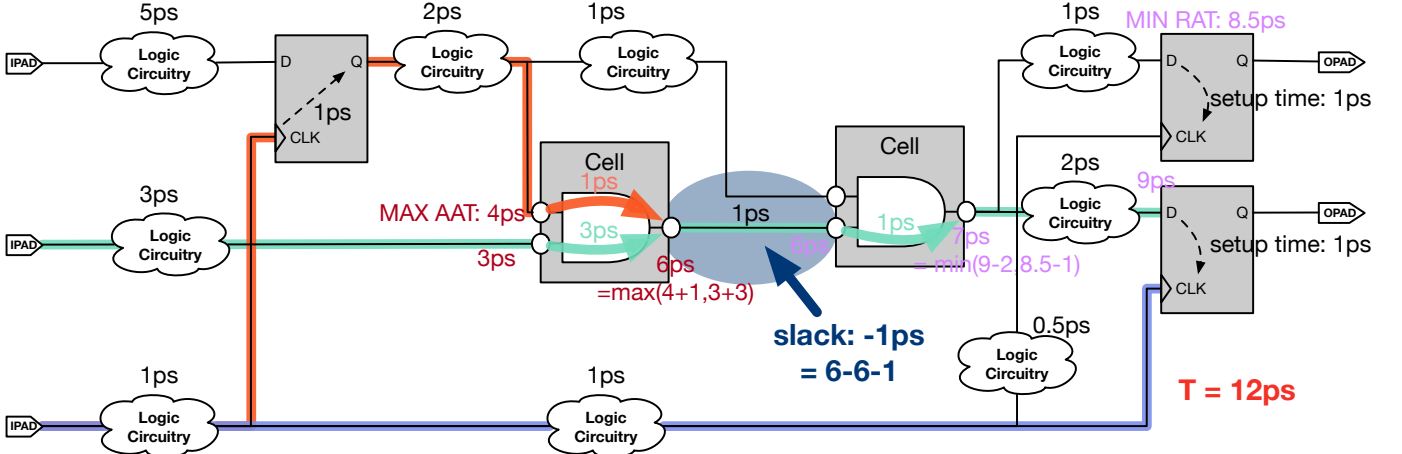


Fig. 8: An illustration for the static timing analysis on FPGA. Support the clock period is  $T$  and the signal arrival time at primary input ports has minor skew. The required arrival time at the sink of a timing path is the clock period minus the clock delay at the capture FFs and the setup time of FFs (1ps in our example), and the required arrival time of a timing endpoint is determined by the required arrival time of its fanout endpoints and the fanout edge delays. The actual arrival time of a timing endpoint is the maximal accumulated delay from the primary inputs. The slack of a timing edge is the difference between the required arrival time at its sink, and the summation of the actual arrival time at its source and its edge delay.

compute the slack from the actual arrival times and required arrival times at timing endpoints [31].

$$T_{ATT}(v_i) = \max_{v_j \in fanin(v_i)} T_{ATT}(v_j) + e_{j,i} \quad (11a)$$

$$T_{ATT}(v_i) = \min_{v_j \in fanout(v_i)} T_{RAT}(v_j) - e_{i,j} \quad (11b)$$

In Eq. (11),  $v_i$  is an endpoint in the timing graph, and  $e_{i,j}$  denotes the timing delays from endpoint  $i$  to endpoint  $j$ , provided by the delay model. The slack of timing edge  $s_{i,j}$  connecting the source endpoint  $v_i$  and the sink endpoint  $v_j$  is

$$s_{i,j} = T_{RAT}(v_j) - T_{ATT}(v_i) - e_{i,j}, \quad (12)$$

Fig. 8 illustrates the timing analysis process.

2) *Timing-driven Net Reweighting Scheme*: In the timing graph, nets have diverse effects on the timing slacks. Those nets with higher timing criticality should be more sensitive to the timing closure. To improve the timing in the analytical placement framework, we assign different net weights to different nets based on their timing criticality. Let  $s_e$  and  $s_{wns}$  denote the timing slacks of net  $e$  and the worst negative slack, respectively. We define the timing criticality  $c_e$  as follows,

$$c_e = \frac{\min(0, s_e)}{\min(0, s_{wns}) - T} \in [0, 1], \quad (13)$$

where  $T$  is the clock period. When net  $e$  is not on a path with timing violation, i.e.  $s_e \geq 0$ , the timing criticality  $c_e$  remains zero. Otherwise, the timing criticality equals the ratio  $\frac{|s_e|}{|s_{wns}| + T}$ . The worse timing slack  $|s_e|$  is, the larger timing criticality  $c_e$  it will have. The largest timing criticality falls upon the nets on the most critical path.

After evaluating the timing criticality, we compute the net weight  $w_e \in \omega$  as

$$\beta_e = \alpha \cdot \max(1, \exp(c_e)) \quad (14a)$$

$$\omega'_e \leftarrow \omega_e \cdot \beta_e \quad (14b)$$

where  $\omega'_e$  is the updated net weight,  $\beta_e$  denotes the reweighting magnitude for net  $e$ , and  $\alpha$  is a hyper-parameter that controls the weighting magnitude <sup>3</sup>.

3) *Effectiveness Analysis of the Reweighting Scheme*: It is suggested that our reweighting scheme can control the reweighting scale according to the severity of the target timing constraints. The reweighting magnitude  $\beta_e$  of a net is determined by the largest magnitude of the timing paths that pass through it, i.e.,  $\beta_e = \max_{\pi \ni e} \beta_{\pi}$ . We then gave a brief analysis of how the timing path  $\pi$  affects the re-weighting scheme in nets.

For the paths with maximal delay  $d_{wns}$ , the intuition is that the reweighting method should make no effect, i.e.,  $\beta_{wns}$  equals 1, when it has no timing violations. Otherwise, the smaller  $T - d_{wns}$  is, the larger the reweighting magnitude should be. Fig. 9a show the relationship between the magnitude of the reweighting  $\beta_{wns}$  and the clock period  $T$  for a certain path and its delay. This figure demonstrates that a path will only gain a reweighting magnitude greater than one when the target clock period  $T$  is less than its path delay. The reweighting magnitude will grow faster with  $T$  becoming smaller. Fig. 9b regards the path delay as a variable and shows how the reweighting magnitude  $\beta_{wns}$  reacts under a certain clock period. The relationship curves align with our intuition that nets with a smaller timing delay always gain a smaller reweighting magnitude. No matter what the clock period is, the reweighting magnitude only takes effect on those paths with timing violations.

Nets on critical paths gain a larger weighting magnitude in this stage. In the subsequent analytical placement step, the increased net weights then help critical paths tilt more toward timing closure in the tradeoff between timing and area.

<sup>3</sup>In our experiments,  $\alpha$  equals 1.

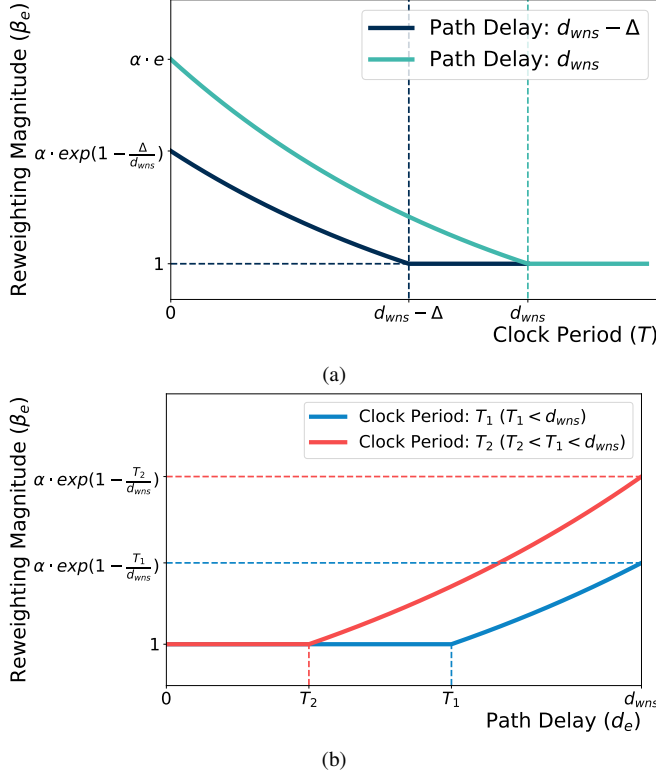


Fig. 9: (a) This figure illustrates the relationship between the reweighting magnitude  $\beta_e$  and the clock period  $T$  given a certain path and its delay. In particular, the path with delay  $d_{wns}$  represents the most critical path. This figure also depicts another path with delay  $d_{wns} - \Delta$ , where  $\Delta$  measures how much the delay is smaller than the worst-case path  $d_{wns}$ . (b) This figure shows the relationship between the reweighting magnitude  $\beta_e$  and the path delay  $d_e$  given a clock period. This figure plots two curves for two certain clock periods  $T_1$  and  $T_2$  ( $T_2 < T_1 < d_{wns}$ ).

#### IV. EXPERIMENTAL RESULTS

We implemented our GPU-accelerated placer in C++ and Python along with the open-source machine learning framework Pytorch for fast gradient back propagation [32]. We conduct experiments on a Ubuntu 18.04 LTS platform that consists of an Intel(R) Xeon(R) Silver 4214 CPU @ 2.20GHz (24 cores), one NVIDIA TITAN GPU, and 251GB memory. We demonstrate the effectiveness and efficiency of our proposed algorithm on both academic benchmarks [17] and industrial benchmarks from the three most concerning aspects of routed wirelength (RWL), runtime (RT), and timing.

##### A. Evaluation on Academic Benchmarks

The statistics of the ISPD 2017 academic benchmark are summarized in TABLE II. The number of instances varies from 400K to 900K with 32–58 clock nets. We do not evaluate the timing performance because on this benchmark we have no access to the timing information of the device. We compare the routed wirelength reported by patched Xilinx Vivado v2016.4 and placement runtime with four state-of-the-art placers, UTPlaceF 2.0 [9], RippleFPGA [11],

UTPlaceF 2.X [10], and NTUfplace [15]. All the results of these placers are from their original placers. We do not compare the results with `elfPlace` because its algorithm cannot handle clock constraints (see TABLE I).

The experimental results show that our placement algorithm consistently achieves better routed wirelengths than other placers. Specifically, our placer achieves 14.2% smaller routed wirelength than UTPlaceF 2.0, 11.7% smaller than RippleFPGA, 9.6% smaller than UTPlaceF 2.X, and 7.9% smaller than NTUfplace on average, respectively. For some benchmarks, like CLK-FPGA06, which is a large design with about 925K cells and 58 clock nets, our routed wirelength is even 13.6%, 6.7%, 10.5% and 4.1% better than that of baseline placers, respectively. It needs to be mentioned that UTPlaceF 2.X is a follow-up work to UTPlaceF 2.0, which relaxes the clock region bounding box constraints to clock tree constraints. It allows for a larger solution space for clock routing feasibility and thus should yield better results. However, even in this unfair comparison, our routed wirelength is still 9.6% better than UTPlaceF 2.X, exhibiting the efficacy of our algorithm. Besides, our GPU-accelerated placer is the fastest one with  $4.94 \times$ ,  $2.38 \times$ ,  $1.45 \times$ , and  $6.58 \times$  speedup over other placers, respectively. These experiments demonstrate the effectiveness and efficiency of our proposed algorithms.

##### B. Evaluation on Industry Benchmarks

We further evaluate our placer on industrial benchmarks which consist of a comprehensive instance set and an industrial FPGA architecture from real-world industry scenarios, including SHIFT, distributed RAM, and CARRY (see TABLE III). Most previous FPGA placers [5], [7], [9]–[11], [13], [15], [21], [23], [24] cannot fully handle such an instance set with SLICEL-SLICEM heterogeneity. To better validate the effectiveness of our placer, we leverage a high-quality FPGA router to evaluate the placement algorithms more precisely [34].

From TABLE III, we can see the comparison between the conference version [33] and our placer. Our placer can achieve 23.6% better WNS and 22.5% better TNS, respectively, with minor routed wirelength degeneration, exhibiting the effectiveness of our placer. In some benchmarks, such as IND06, which is one of the most congestion benchmarks, our WNS and TNS are 40.8% and 51.2% better than the baseline, respectively. These experiments demonstrate that our placer can effectively optimize timing even on congested benchmarks. The experiments also show that our placer requires more time to converge on industrial benchmarks. This is because optimizing timing requires additional iterations, which needs further optimization in the future.

##### C. Ablation Study for Optimization Techniques

To better understand the performance of our placer, we perform an ablation study and validate the effectiveness of our proposed methods by disabling optimization techniques as follows (see TABLE IV).

TABLE II: Routed Wirelength ( $\times 10^3$ ) and Runtime (Seconds) Comparison on ISPD 2017 Benchmarks.

Design	#LUT/#FF/#BRAM/#DSP	#Clock	UTPlaceF 2.0 [9]	RWL	RT	RippleFPGA [11]	RWL	RT	UTPlaceF 2.X [10]	RWL	RT	NTUfplace [15]	RWL	RT	Ours (GPU)	RWL	RT
CLK-FGPA01	211K/324K/164/75	32	2208	532	2011	288	2092	180	2039	698	1868	136					
CLK-FGPA02	230K/280K/236/112	35	2279	513	2168	266	2194	179	2149	710	2011	130					
CLK-FGPA03	410K/481K/850/395	57	5353	1039	5265	583	5109	343	4901	1704	4755	215					
CLK-FGPA04	309K/372K/467/224	44	3698	711	3607	380	3600	242	3614	1148	3338	162					
CLK-FGPA05	393K/469K/798/150	56	4692	939	4660	569	4556	323	4417	1540	4154	208					
CLK-FGPA06	425K/511K/872/420	58	5589	1066	5737	591	5432	346	5122	2210	4918	229					
CLK-FGPA07	254K/309K/313/149	38	2444	845	2326	304	2324	201	2320	795	2145	141					
CLK-FGPA08	212K/257K/161/75	32	1886	529	1778	247	1807	169	1803	588	1648	120					
CLK-FGPA09	231K/358K/236/112	35	2601	842	2530	327	2507	197	2436	717	2248	144					
CLK-FGPA10	327K/506K/542/255	47	4464	974	4496	512	4229	286	4339	1597	3839	200					
CLK-FGPA11	300K/468K/454/224	44	4183	1068	4190	455	3936	265	3964	1618	3626	183					
CLK-FGPA12	277K/430K/389/187	41	3369	774	3388	409	3236	247	3179	849	2938	168					
CLK-FGPA13	339K/405K/570/262	47	3816	1172	3833	441	3723	270	3680	985	3404	181					
Ratio				1.142	4.943	1.117	2.379	1.096	1.453	1.079	6.575	1.000	1.000	1.000	1.000	1.000	1.000

 TABLE III: Routed Wirelength ( $\times 10^3$ ), WNS ( $\times 10^3$  ps), TNS ( $\times 10^5$  ps) and Runtime (Seconds) Comparison between Conference Version and Our Algorithm on Industry Benchmarks.

Design	#LUT/#FF/#BRAM/#DSP	#DistributedRAM+#SHIFT	#CARRY	ClockPeriod	Conference Version [33]				Ours (GPU)			
					RWL	WNS	TNS	RT	RWL	WNS	TNS	RT
IND01	17K/11K/0/13	9	2K	5	90	-3.941	-2.422	45	90	-1.751	-1.323	70
IND02	11K/10K/0/24	6	335	2	102	-4.240	-19.733	54	117	-2.938	-18.148	76
IND03	109K/12K/0/0	0	0	3	1028	-2.666	-18.467	59	1031	-2.764	-16.836	144
IND04	29K/17K/0/16	218	1K	5	279	-5.399	-27.915	83	283	-6.382	-21.112	88
IND05	64K/191K/64/928	29K	4K	10	2305	-10.306	-3.009	97	2312	-4.558	-2.354	218
IND06	112K/65K/21/0	0	4K	15	1585	-10.987	-106.384	84	1585	-6.502	-51.922	193
IND07	40K/156K/89/768	26K	3K	4	1498	-6.302	-20.585	83	1505	-6.039	-21.030	265
Ratio					1.000	1.000	1.000	1.000	1.025	0.764	0.775	2.029

 TABLE IV: Routed Wirelength( $\times 10^3$ ), WNS ( $\times 10^3$  ps), TNS ( $\times 10^5$  ps), and Runtime (Seconds) Comparison with Different Techniques on Industry Benchmarks.

Design	w/o precond or chain align(GPU)				w/o precond(GPU)				w/o chain align(GPU)				Ours(GPU)			
	RWL	WNS	TNS	RT	RWL	WNS	TNS	RT	RWL	WNS	TNS	RT	RWL	WNS	TNS	RT
IND01	103	-3.491	-2.849	53	94	-3.041	-1.826	66	108	-2.581	-143.009	74	90	-1.751	-1.323	70
IND02	124	-4.580	-28.426	148	180	-4.827	-43.930	64	118	-6.449	-6029.390	73	117	-2.938	-18.148	76
IND03	1021	-3.080	-17.301	123	1021	-3.080	-17.301	126	1030	-2.604	-1776.630	125	1031	-2.764	-16.836	144
IND04	377	-9.384	-28.074	88	392	-8.808	-31.798	90	290	-4.288	-610.918	76	283	-6.382	-21.112	88
IND05	2290	-4.502	-3.702	137	diverge	diverge	diverge	diverge	2260	-4.870	-238.678	153	2312	-4.558	-2.354	218
IND06	1558	-50.647	-105.558	109	1576	-11.450	-113.733	107	1580	-15.977	-5320.100	114	1585	-6.502	-51.922	193
IND07	1547	-9.470	-31.747	186	1393	-8.145	-20.816	155	diverge	diverge	diverge	diverge	1505	-6.039	-21.030	265
Ratio	1.076	2.355	1.599	0.922	1.147	1.497	1.586	0.801	1.034	1.468	1.298	0.837	1.000	1.000	1.000	1.000

- Disable the iterative carry chain alignment correction in global placement and only align chains once in legalization.
- Disable the dynamic preconditioner and use the default preconditioner in [13], [30].
- Disable both techniques as the baseline.

We can see from TABLE IV that both the iterative carry chain alignment correction technique and dynamically-adjusted preconditioner technique helps stabilize the global placement convergence and enables better placement solution at convergence. Without either of these two techniques, the placer fails to converge on one design. The dynamically-adjusted preconditioner helps achieve 14.7% better routed wirelength, 49.7% better WNS, and 58.6% better TNS compared with the default preconditioner [13], [30]. Moreover, the iterative carry chain alignment correction helps optimize the routed wirelength, WNS, and TNS by 3.4%, 46.8%, and 29.8% with minor runtime overhead. These experiments validate the effectiveness and efficacy of the proposed carry chain alignment and preconditioning technique.

#### D. Runtime Breakdown

To analyze the time consumption of our placer, we further exhibit the runtime breakdown of our algorithm on one of the largest benchmarks as shown in Fig. 10. With the help of GPU acceleration, global placement is no longer the most time-consuming part. The core forward and backward propagation of the global placement, i.e., the computation of wirelength and electrostatic density, as well as their gradients, only take up 26% and 17% of the global placement runtime, respectively. With the great reduction in global placement runtime, legalization becomes the new runtime bottleneck, taking 53% of the total placement time. Meanwhile, other miscellaneous parts, including IOs, parsing, database establishment, etc., take up also the same time as that of global placement.

## V. CONCLUSION

In this paper, we present a heterogeneous FPGA placement algorithm that considers the heterogeneity of SLICELs and SLICEMs, as well as timing closure and clock feasibility. A new electrostatic formulation and a nested Lagrangian paradigm have been proposed to achieve uniform optimization of wirelength, routability, timing, and clock feasibility for

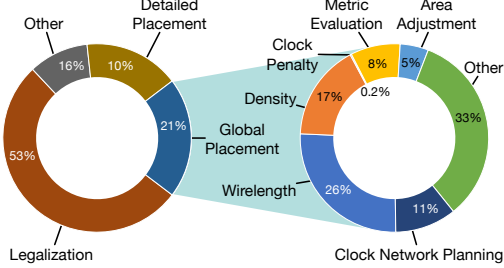


Fig. 10: Runtime breakdown on CLK-FPGA13. Similar distributions are observed on other benchmarks.

heterogeneous instance types, including LUT, FF, BRAM, DSP, distributed RAM, SHIFT, and CARRY. Additionally, we propose a dynamically adjusted preconditioner, a timing-driven net-weighting scheme, and a smooth clock penalization technique in order to ensure that the placement is convergent to high-quality solutions. On the ISPD 2017 contest benchmark, experiments have revealed that our placer can achieve 14.2%, 11.7%, 9.6%, and 7.9% better routed wirelengths compared to the state-of-the-art placers, UTPlaceF 2.0, RippleFPGA, UTPlaceF 2.X, and NTUFplace, respectively, at 1.5–6× speedup leveraging GPU acceleration. We conducted experiments on industrial benchmarks to prove that our algorithms are capable of achieving 23.6% better WNS and 22.5% better TNS with about 2% increase in routed wirelength.

## REFERENCES

- [1] S.-J. Lee and K. Raahemifar, “Fpga placement optimization methodology survey,” in *Canadian Conference on Electrical and Computer Engineering (CCECE)*. IEEE, 2008, pp. 001 981–001 986.
- [2] I. L. Markov, J. Hu, and M.-C. Kim, “Progress and challenges in VLSI placement research,” *Proceedings of the IEEE*, vol. 103, no. 11, pp. 1985–2003, 2015.
- [3] P. Maidee, C. Ababei, and K. Bazargan, “Timing-driven partitioning-based placement for island style fpgas,” *IEEE TCAD*, vol. 24, no. 3, pp. 395–406, 2005.
- [4] S. Chen and Y. Chang, “Routing-architecture-aware analytical placement for heterogeneous fpgas,” in *Proc. DAC*. ACM, 2015, pp. 27:1–27:6.
- [5] W. Li, S. Dhar, and D. Z. Pan, “Utplacef: A routability-driven FPGA placer with physical and congestion aware packing,” *IEEE TCAD*, vol. 37, no. 4, pp. 869–882, 2018.
- [6] C. Pui, G. Chen, W. Chow, K. Lam, J. Kuang, P. Tu, H. Zhang, E. F. Y. Young, and B. Yu, “Ripplefpga: a routability-driven placement for large-scale heterogeneous fpgas,” in *Proc. ICCAD*, 2016, p. 67.
- [7] R. Pattison, Z. Abuwaimer, S. Areibi, G. Gréwal, and A. Vannelli, “Gplace: a congestion-aware placement tool for ultrascale fpgas,” in *Proc. ICCAD*, 2016, p. 68.
- [8] W. Li and D. Z. Pan, “A new paradigm for FPGA placement without explicit packing,” *IEEE TCAD*, vol. 38, no. 11, pp. 2113–2126, 2019.
- [9] W. Li, Y. Lin, M. Li, S. Dhar, and D. Z. Pan, “Utplacef 2.0: A high-performance clock-aware FPGA placement engine,” *ACM TODAES*, vol. 23, no. 4, pp. 42:1–42:23, 2018.
- [10] W. Li, M. E. Dehkordi, S. Yang, and D. Z. Pan, “Simultaneous placement and clock tree construction for modern fpgas,” in *Proc. FPGA*, 2019, pp. 132–141.
- [11] C. Pui, G. Chen, Y. Ma, E. F. Y. Young, and B. Yu, “Clock-aware ultrascale FPGA placement with machine learning routability prediction: (invited paper),” in *Proc. ICCAD*. IEEE, 2017, pp. 929–936.
- [12] T. Liang, G. Chen, J. Zhao, L. Feng, S. Sinha, and W. Zhang, “Amfplacer: High-performance analytical mixed-size placer for fpga,” in *Proc. ICCAD*, 2021, pp. 1–6.
- [13] Y. Meng, W. Li, Y. Lin, and D. Z. Pan, “elfplace: Electrostatics-based placement for large-scale heterogeneous fpgas,” *IEEE TCAD*, 2021.
- [14] Y. Kuo, C. Huang, S. Chen, C. Chiang, Y. Chang, and S. Kuo, “Clock-aware placement for large-scale heterogeneous fpgas,” in *Proc. ICCAD*, 2017, pp. 519–526.
- [15] J. Chen, Z. Lin, Y. Kuo, C. Huang, Y. Chang, S. Chen, C. Chiang, and S. Kuo, “Clock-aware placement for large-scale heterogeneous fpgas,” *IEEE TCAD*, vol. 39, no. 12, pp. 5042–5055, 2020.
- [16] S. Yang, A. Gayasen, C. Mulpuri, S. Reddy, and R. Aggarwal, “Routability-driven FPGA placement contest,” in *Proc. ISPD*, 2016, pp. 139–143.
- [17] S. Yang, C. Mulpuri, S. Reddy, M. Kalase, S. Dasasathyan, M. E. Dehkordi, M. Tom, and R. Aggarwal, “Clock-aware FPGA placement contest,” in *Proc. ISPD*, 2017, pp. 159–164.
- [18] M.-C. Kim, N. Viswanathan, Z. Li, and C. Alpert, “ICCAD-2013 CAD contest in placement finishing and benchmark suite,” in *Proc. ICCAD*, 2013, pp. 268–270.
- [19] Ultrascale architecture clb slices. [Online]. Available: [https://www.xilinx.com/support/documentation/user\\_guides/ug574-ultrascale-clb.pdf](https://www.xilinx.com/support/documentation/user_guides/ug574-ultrascale-clb.pdf)
- [20] T. Martin, D. Maarouf, Z. Abuwaimer, A. Alhyari, G. Gréwal, and S. Areibi, “A flat timing-driven placement flow for modern fpgas,” in *Proc. DAC*. ACM, 2019, p. 4.
- [21] Z. Lin, Y. Xie, G. Qian, J. Chen, S. Wang, J. Yu, and Y.-W. Chang, “Timing-driven placement for fpgas with heterogeneous architectures and clock constraints,” in *Proc. DATE*. IEEE, 2021, pp. 1564–1569.
- [22] A. Marquardt, V. Betz, and J. Rose, “Timing-driven placement for fpgas,” in *Proc. FPGA*. ACM, 2000, pp. 203–213.
- [23] G. Chen, C.-W. Pui, W.-K. Chow, K.-C. Lam, J. Kuang, E. F. Young, and B. Yu, “RippleFPGA: Routability-driven simultaneous packing and placement for modern FPGAs,” *IEEE TCAD*, vol. 37, no. 10, pp. 2022–2035, 2018.
- [24] Z. Abuwaimer, D. Maarouf, T. Martin, J. Foxcroft, G. Gréwal, S. Areibi, and A. Vannelli, “GPlace3.0: Routability-driven analytic placer for UltraScale FPGA architectures,” *ACM TODAES*, vol. 23, no. 5, pp. 66:1–66:33, 2018.
- [25] Ultrascale architecture clocking resources. [Online]. Available: [https://www.xilinx.com/support/documentation/user\\_guides/ug572-ultrascale-clocking.pdf](https://www.xilinx.com/support/documentation/user_guides/ug572-ultrascale-clocking.pdf)
- [26] J. Lu, P. Chen, C.-C. Chang, L. Sha, D. J.-H. Huang, C.-C. Teng, and C.-K. Cheng, “ePlace: Electrostatics-based placement using fast fourier transform and nesterov’s method,” *ACM TODAES*, vol. 20, no. 2, p. 17, 2015.
- [27] A. B. Kahng, S. Mantik, and I. L. Markov, “Min-max placement for large-scale timing optimization,” in *Proc. ISPD*, 2002, pp. 143–148.
- [28] J. Lu, H. Zhuang, P. Chen, H. Chang, C.-C. Chang, Y.-C. Wong, L. Sha, D. Huang, Y. Luo, C.-C. Teng *et al.*, “ePlace-MS: Electrostatics-based placement for mixed-size circuits,” *IEEE TCAD*, vol. 34, no. 5, pp. 685–698, 2015.
- [29] R. Andreani, E. G. Birgin, J. M. Martínez, and M. L. Schuverdt, “On augmented lagrangian methods with general lower-level constraints,” *SIAM Journal on Optimization*, vol. 18, no. 4, pp. 1286–1309, 2008.
- [30] C.-K. Cheng, A. B. Kahng, I. Kang, and L. Wang, “Replace: Advancing solution quality and routability validation in global placement,” *IEEE TCAD*, 2018.
- [31] T. Huang and M. D. F. Wong, “Opentimer: A high-performance timing analysis tool,” in *Proc. ICCAD*. IEEE, 2015, pp. 895–902.
- [32] Y. Lin, Z. Jiang, J. Gu, W. Li, S. Dhar, H. Ren, B. Khailany, and D. Z. Pan, “DREAMPlace: Deep learning toolkit-enabled gpu acceleration for modern vlsi placement,” *IEEE TCAD*, June 2020.
- [33] J. Mai, Y. Meng, Z. Di, and Y. Lin, “Multi-electrostatic fpga placement considering slice-slicem heterogeneity and clock feasibility,” in *Proc. DAC*, 2022, pp. 649–654.
- [34] J. Wang, J. Mai, Z. Di, and Y. Lin, “A robust fpga router with concurrent intra-clb rerouting,” in *Proc. ASPDAC*, 2023, pp. 529–534.